Geochemical Perspectives Letters

Brucite formation and dissolution in oceanic serpentinite

F. Klein, S.E. Humphris, W. Bach

Supplementary Information

The Supplementary Information includes:

- Analytical Methods
- Rock Description
- Figures S-1 and S-2
- Tables S-1 and S-2
- Supplementary Information References

Analytical Methods

Raman spectroscopy was conducted at Woods Hole Oceanographic Institution using a Horiba LabRam HR system equipped with 3 lasers (473 nm, 532 nm, 633 nm), two gratings (600, 1800 grooves per mm), and an Olympus BX41 microscope. The instrument was calibrated using the 520.7 cm^{-1} band of Si before each session and checked for drift every two hours. Most analyses were carried out using the 633 nm laser between 100 and 1280 cm^{-1}. To unequivocally distinguish serpentine minerals, additional analyses were conducted between 3500 and 3800 cm^{-1}. Spectra were processed with the Labspec 6 software suite for background subtraction and compared with reference spectra (Downs, 2006; Petriglieri *et al.*, 2015) for mineral identification.

A TA Instruments Q600 simultaneous thermal analyser was used at Woods Hole Oceanographic Institution for differential scanning calorimetry and thermogravimetric analysis to determine the presence and amounts of brucite and serpentine. We adopted this approach from previous studies that successfully used thermogravimetry to determine the abundances of serpentine and brucite formed during hydrothermal laboratory experiments (Okamoto *et al.*, 2011; Lafay *et al.*, 2012). The mass loss due to dehydroxylation of brucite, i.e. $Mg(OH)_2 \rightarrow MgO + H_2O$ is proportional to the abundance of brucite in a sample. Likewise, the mass loss due to dehydroxylation of serpentine ($Mg_3Si_2O_5(OH)_4$) is

proportional to the abundance of serpentine in a sample. While dehydroxylation of serpentine is complete at 750°C, its decomposition involves a series of reaction products including talc ($Mg_3Si_4O_{10}(OH)_2$ and forsterite (Mg_2SiO_4); *i.e.*, $5Mg_3Si_2O_5(OH)_4 \rightarrow Mg_3Si_4O_{10}(OH)_2 + 6Mg_2SiO_4 + 9H_2O$, and, in a second step, talc reacts with forsterite to form enstatite ($MgSiO_3$); *i.e.*, $Mg_3Si_4O_{10}(OH)_2 + Mg_2SiO_4 \rightarrow 5MgSiO_3 + H_2O$ (Gualtieri *et al.*, 2012). As shown in Figure 1, the dehydroxylation of brucite and serpentine take place over discrete temperature intervals, which can be conveniently used to determine their abundances. Any mass loss between 250 and 450°C was attributed to dehydroxylation of brucite, whereas any mass loss between 450 and 750°C was attributed to dehydroxylation of serpentine (Fig. 1). Molar proportions and concentrations of serpentine and brucite of individual samples were calculated by assuming that the molar X_{Mg} (Mg/(Mg+Fe)) of brucite was 0.8 and that of serpentine was 0.95, with molar masses of 64.63 g/mol and 281.84 g/mol, respectively. This assumption is simplistic considering the Fe contents of these minerals are variable; however, such variations have a negligible effect on calculated molar serpentine / brucite ratios. Except for the dehydroxylation of iowaite, which forms at the expense of brucite without modifying its (Mg+Fe)/OH ratio, no other minerals underwent dehydroxylation between 250 and 450 °C. Chlorite, which commonly occurs as an accessory mineral in bastite texture, would show characteristic dehydroxylation patterns between 460 and 865 °C (Földvári, 2011) that were not observed in our measurements. Hence, the possible presence of trace amounts of chlorite did not affect the interpretation of our data to any significant extent.

For each analysis, 20-50 mg of finely powdered material was heated from room temperature to 1100°C (heating rate = 10°C per minute) in a N_2 atmosphere (flow rate = 50 mL per minute). Repeated measurements of standard materials supplied by the manufacturer suggest that the temperature is accurate to 1°C and the weight change to 0.5 µg. Brucite-free serpentinite showed an average baseline weight loss of 0.9% between 250 and 450°C, which was subtracted from the measured values over this temperature interval for calculation of brucite contents. Based on repeat analyses, the limit of quantification for mass loss of water from hydrous minerals was better than 0.1 wt.%, which would correspond to 0.4 wt. % brucite with the composition $Mg_{0.8}Fe_{0.2}(OH)_2$.

Major elements of dredged samples were analysed using X-ray fluorescence (XRF) at the Peter Hooper GeoAnalytical Lab at the Washington State University (Pullman, WA) (Johnson *et al.*, 1999). Loss on ignition (LOI) was also measured at the GeoAnalytical Lab by heating the dredged samples in ceramic crucibles to 900 °C. Major element data of drilled samples examined in this study are taken from Klein *et al*. (2017).

Equilibrium constants for dissolution of minerals displayed in Figure 4 were calculated using the modelling code SUPCRT92 (Johnson *et al.*, 1992) using a customised database that contains thermodynamic data of minerals and aqueous species. Details of this database are provided elsewhere (Klein *et al.*, 2009, 2013).

Rock Description

Protoliths of serpentinites included mostly harzburgite and dunite. The extent of serpentinisation ranged from incipient in peridotite mylonite to complete in protogranular peridotite. Serpentinisation involved the formation of the serpentine group minerals lizardite and chrysotile, as well as antigorite in samples from the Mariana forearc. Magnetite is more abundant in samples from mid-ocean ridges that formed at relatively high temperatures than in samples from passive margins and subduction zone forearcs. Talc and chlorite are accessories in bastite texture of some serpentinites from mid-ocean-ridge settings; however, we did not include samples that underwent extensive talc-alteration in this study. The occurrence of brucite was previously established in select samples that were recovered by seafloor drilling using electron microprobe analysis and confocal Raman spectroscopy (Klein *et al.*, 2009, 2014; Kahl *et al.*, 2015; Nielsen *et al.*, 2015). Evidence for several serpentinisation events was commonly expressed through cross-cutting veins of distinct generations in all samples. Some of the dredged samples showed visible signs of weathering, such as orange-red staining and weathering rinds. To examine differences in weathering extent, samples from the weathering rind (halo) and the sample interior were analysed (sample IO11-76 60 171a & IO11-76 60 171b). Some of the dredged samples showed visible evidence for extensive to pervasive weathering (K162-9 30-105, CHN35 7-92, VULC-5 41-29, OCE-23 14-1. AII107-6 40-31) whereas others did not appear to be weathered (K162-9 45-25, K162-9 58-33, CHN35 7-383, CHN35 7-15, CHN35 18-109, CHN35 18-287, IO11-76 60-27, IO11-76 60-60, IO11-76 60-165, VULC-5 41-13, OCE-23 14-3, AII107-6 40-46). However, TGA-DSC revealed that all of the dredged samples had undergone weathering, even the seemingly unweathered ones.

Supplementary Figures

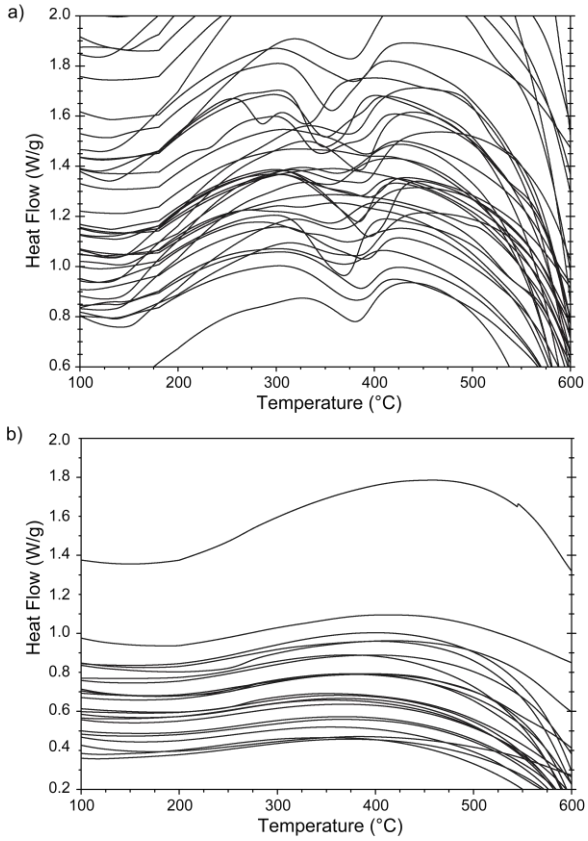

Figure S-1 Differential scanning calorimetry of drilled **(a)** and dredged **(b)** serpentinites. Drilled serpentinites show a pronounced negative (endothermic) heat flow anomaly between 300 and 400 °C attributed to Fe-bearing brucite. In contrast, dredged serpentinites do not show an endothermic heat flow anomaly, indicating that these samples do not contain brucite.

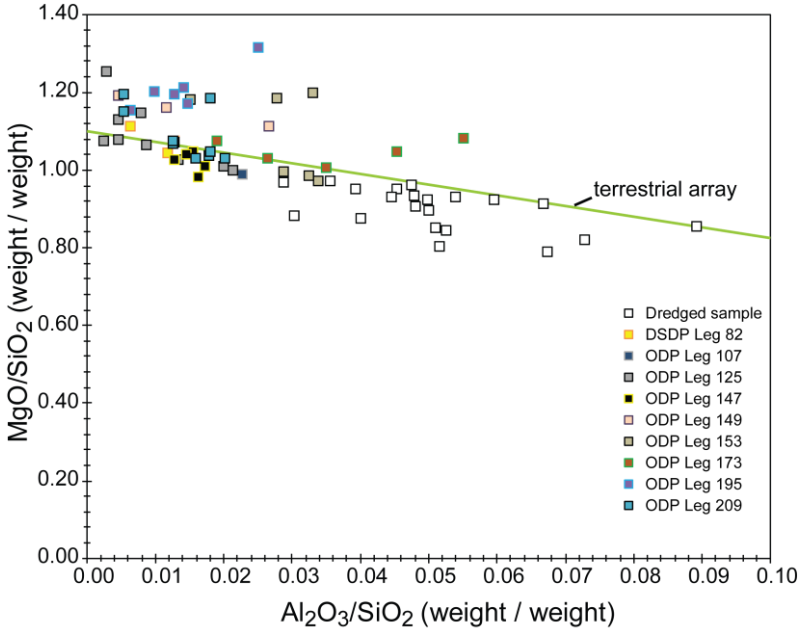

Figure S-2 Major element ratios of samples examined in this study. The terrestrial array (Hart and Zindler, 1986; Jagoutz *et al.*, 1979) is shown for comparison. Drilled samples scatter around the terrestrial array whereas dredged samples fall below it. The decreased MgO/SiO_2 of dredged samples is attributed to loss of Mg. The addition of Si would shift both MgO/SiO_2 and Al_2O_3/SiO_2 to lower values; however, such a trend is not evident. Whole rock major element data of serpentinised peridotites recovered by seafloor drilling are taken from previous studies of the same samples (Paulick *et al.*, 2006; Klein *et al.*, 2017).

Supplementary Tables

Table S-1 Summary of thermogravimetric analysis and molar Mg/Si.

Sample ID	*Area*	*Meters below seafloor [$] (drilled samples)*	*Weight loss (%) 250-450 °C*	*Weight loss (%) 450-750 °C*	*Brucite** (wt.%)*	*MgO from brucite (wt.%)*	*molar Srp/Brc ratio*	*Molar Mg/Si of whole rock**	**Primary DTG peak at temperature (˚C)**	**Secondary DTG peak**
Drilled Samples										
082-558Z-42R-1W, 9-11	Azores, off axis	130.09	1.38	11.11	4.06	2.03	4.03	1.55	313	276
082-558Z-42R-1W, 133-135	Azores, off axis	131.33	2.27	11.64	7.25	3.62	2.56	1.60	325	280
082-558Z-43R-1W, 45-46	Azores, off axis	139.45	3.02	10.59	9.94	4.96	1.75	1.66	315	284
107-651A-57R-2W, 140-142	Tyrrhenian Sea	146.40	1.24	10.62	3.56	1.78	4.28	1.47	276	319
125-779A-03R-1W, 26-28	Conical Seamount	10.86	3.33	10.38	11.06	5.52	1.56	1.71	357	shoulder
125-779A-05R-2W, 35-38	Conical Seamount	31.40	3.31	9.52	10.98	5.48	1.44	1.60	374	shoulder
125-779A-08R-1W, 45-47	Conical Seamount	58.95	2.40	7.51	7.72	3.85	1.56	1.53	388	shoulder
125-779A-10R-2W, 51-53	Conical Seamount	79.44	3.54	9.74	11.81	5.89	1.38	1.60	392	-
125-779A-13R-2W, 46-48	Conical Seamount	108.56	2.19	7.79	6.97	3.48	1.78	1.49	385	-
125-779A-17R-4W, 32-34	Conical Seamount	149.94	1.64	4.24	4.99	2.49	1.29	1.59	378	-
125-779A-25R-1W, 88.5-91	Conical Seamount	197.69	4.60	9.16	15.61	7.79	1.00	1.87	389	-
125-779A-26R-2W, 72-74	Conical Seamount	208.16	1.85	10.27	5.75	2.87	2.78	1.50	384	shoulder
125-779A-33R-2W, 80-82	Conical Seamount	275.32	2.68	10.61	8.73	4.36	1.98	1.59	344	shoulder
125-779A-35R-1W, 22-24	Conical Seamount	293.52	3.74	9.60	12.53	6.25	1.28	1.68	365	-
147-895D-2R-1W, 29-31	Hess Deep	16.29	1.75	7.11	5.39	2.69	2.03	1.46	362	-
147-895D-3R-1W, 64-66	Hess Deep	26.64	2.19	7.53	6.97	3.48	1.72	1.56	377	-
147-895D-4R-3W, 114-116	Hess Deep	38.13	1.90	6.10	5.93	2.96	1.61	1.53	379	-
147-895D-5R-1W, 121-123	Hess Deep	44.51	1.75	6.15	5.39	2.69	1.76	1.50	375	-
147-895D-7R-3W, 13-15	Hess Deep	67.66	2.41	9.12	7.76	3.87	1.89	1.55	371	-
149-897D-23R-1W, 17-20	Iberian Margin	115.37	2.97	10.63	9.76	4.87	1.79	1.65	365	shoulder
149-897D-23R-2W, 63-64	Iberian Margin	117.13	3.80	10.39	12.74	6.36	1.37	1.77	351	shoulder
149-897D-24R-3W, 103-106	Iberian Margin	127.95	3.21	10.41	10.63	5.30	1.62	1.73	344	shoulder
153-920B-1W-3W, 64-66	MARK	3.12	0.49	10.95	-	-	-	1.48	-	-
153-920B-2R-1W, 80-82	MARK	14.80	0.35	10.99	-	-	-	1.47	-	-
153-920B-10R-1W, 82-86	MARK	89.92	0.39	11.37	-	-	-	1.78	-	-
153-920B-10R-2W, 68-70	MARK	91.14	0.53	11.12	-	-	-	1.45	-	-
153-920B-12R-2W, 140-143	MARK	110.55	3.72	10.08	12.46	6.21	1.35	1.76	382.00	334

Table S-1 cont.

Sample ID	*Area*	*Meters below seafloor [$] (drilled samples)*	*Weight loss (%) 250-450 °C*	*Weight loss (%) 450-750 °C*	*Brucite** (wt.%)*	*MgO from brucite (wt.%)*	*molar Srp/Brc ratio*	*Molar Mg/Si of whole rock**	Primary DTG peak at temperature (˚C)	Secondary DTG peak
173-1068A-22R-1W, 30-33	Iberian Margin	3.67	0.99	10.67	-	-	-	1.50	-	
173-1068A-24R-1W, 73-74	Iberian Margin	32.80	2.50	11.00	8.07	4.03	2.20	NA	372.00	shoulder
173-1068A-24R-2W, 56-59	Iberian Margin	33.84	2.70	10.49	8.80	4.39	1.94	1.61	377.00	shoulder
173-1068A-25R-1W, 104-106	Iberian Margin	42.54	2.38	10.79	7.65	3.82	2.27	1.56	363.00	shoulder
173-1068A-26R-1W, 14-16	Iberian Margin	46.01	2.74	11.01	8.94	4.46	2.01	1.60	355.00	shoulder
173-1068A-28R-1W, 49-50	Iberian Margin	55.76	2.17	10.79	6.89	3.44	2.49	1.53	350.00	shoulder
195-1200A-11R-1W, 47-49	South Chamorro	89.87	3.42	10.35	11.37	5.67	1.51	1.78	384.00	shoulder
195-1200A-13R-1W, 121-124	South Chamorro	109.91	3.24	10.08	10.72	5.35	1.56	1.80	379.00	-
195-1200A-16R-2W, 48-50	South Chamorro	139.43	2.73	11.08	8.91	4.45	2.03	1.79	360.00	-
195-1200A-7R-2W, 127-129	South Chamorro	52.96	4.12	9.99	13.89	6.93	1.21	1.96	378.00	-
195-1200A-3R-1W, 3-7	South Chamorro	18.23	2.54	10.55	8.21	4.10	2.08	1.72	373.00	-
195-1200A-17G-2W, 76-79	South Chamorro	unknown	3.17	9.92	10.46	5.22	1.57	1.74	379.00	shoulder
209-1271A_4R2_5-15	MAR 15°20 FZ	29.75	3.04	9.66	10.02	5.00	1.59	1.77	363.00	-
209-1271B_17R1_61-69	MAR 15°20 FZ	85.11	3.05	9.98	10.05	5.01	1.64	1.78	341.00	shoulder
209-1272A_14R1_43-53	MAR 15°20 FZ	66.13	1.62	11.22	4.92	2.46	3.46	1.54	332.00	282
209-1272A_21R1_88-100	MAR 15°20 FZ	99.78	1.99	11.13	6.25	3.12	2.80	1.59	325.00	282
209-1272A_27R2_78-88	MAR 15°20 FZ	129.28	2.43	9.32	7.83	3.91	1.92	1.56	322.00	280
209-1274A_6R3_24-34	MAR 15°20 FZ	33.06	1.91	7.48	5.96	2.97	1.96	1.53	383.00	shoulder
209-1274A_16R2_26-38	MAR 15°20 FZ	85.40	3.06	10.75	10.09	5.03	1.76	1.71	338.00	shoulder
209-1274A_24R1_16-26	MAR 15°20 FZ	131.96	1.36	10.66	3.99	1.99	3.92	1.70	316.00	-
209-1274A_27R1_130-140	MAR 15°20 FZ	147.40	2.43	8.92	7.83	3.91	1.84	1.60	346.00	shoulder
Dredged samples										
K162-9 30-105	SWIR, Oblique SC		0.84	8.28	-	-	-	1.21	-	-
K162-9 45-25	SWIR, Oblique SC		1.03	11.22	-	-	-	1.43	-	-
K162-9 58-23	SWIR, Oblique SC		0.53	7.61	-	-	-	1.17	-	-
K162-9 58-33	SWIR, Oblique SC		0.83	10.15	-	-	-	1.35	-	-
CHN35 7-15	MAR St. Paul's Rocks		0.54	2.54	-	-	-	1.39	-	-
CHN35 7-92	MAR St. Paul's Rocks		0.69	7.84	-	-	-	1.38	-	-
CHN35 7-383	MAR St. Paul's Rocks		0.25	1.00	-	-	-	1.42	-	-

Table S-1 cont.

Sample ID	*Area*	*Meters below seafloor $ (drilled samples)*	*Weight loss (%) 250-450 °C*	*Weight loss (%) 450-750 °C*	*Brucite** (wt.%)*	*MgO from brucite (wt.%)*	*molar Srp/Brc ratio*	*Molar Mg/Si of whole rock**	Primary DTG peak at temperature (˚C)	Secondary DTG peak
CHN35 18-109	MAR St. Paul's Rocks		0.30	6.21	-	-	-	1.27	-	-
CHN35 18-287	MAR St. Paul's Rocks		0.35	9.15	-	-	-	1.36	-	-
IO11-76 60-27	SWIR Islas Orcadas FZ		0.74	9.20	-	-	-	1.37	-	-
IO11-76 60-51	SWIR Islas Orcadas FZ		0.81	7.42	-	-	-	1.19	-	-
IO11-76 60-60	SWIR Islas Orcadas FZ		0.87	10.68	-	-	-	1.42	-	-
IO11-76 60-165	SWIR Islas Orcadas FZ		0.88	10.54	-	-	-	1.38	-	-
IO11-76 60-171a	SWIR Islas Orcadas FZ		0.75	11.08	-	-	-	1.44	-	-
IO11-76 60-171b	SWIR Islas Orcadas FZ		0.91	10.30	-	-	-	1.39	-	-
VULC-5 35-37	SAAR Bullard FZ		0.68	7.63	-	-	-	1.30	-	-
VULC-5 41-13	SAAR Bullard FZ		1.03	7.88	-	-	-	1.22	-	-
VULC-5 41-29	SAAR Bullard FZ		0.67	6.96	-	-	-	1.27	-	-
OCE-23 14-1	Mid-Cayman Rise		0.80	6.89	-	-	-	1.26	-	-
OCE-23 14-3	Mid-Cayman Rise		0.56	8.48	-	-	-	1.33	-	-
AII107-6 40-31	SWIR Bouvet FZ		0.87	8.56	-	-	-	1.31	-	-
AII107-6 40-46	SWIR Bouvet FZ		0.71	10.90	-	-	-	1.44	-	-

$ refers to igneous basement not counting sediments, ** reported brucite contents include minor iowaite recalculated as brucite, * molar ratio of whole rocks from X-ray fluorescence, wt.% = weight percent, DTG = 1st derivative of weight loss, NA = not analysed, MARK = Mid-Atlantic Ridge Kane fracture zone area, MAR = Mid-Atlantic Ridge, FZ = fracture zone, SWIR = Southwest Indian Ridge, SC = spreading center, SAAR = South American Antarctic Ridge

Table S-2 X-ray fluorescence analysis of major elements in dredged samples.

Sample #	SiO_2 wt. %	Al_2O_3 wt. %	TiO_2 wt. %	FeO wt. %	MnO wt. %	CaO wt. %	MgO wt. %	K_2O wt. %	Na_2O wt. %	P_2O_5 wt. %	Total wt. %	Loss on Ignition wt. %
K162-9 30-105	46.88	2.93	0.056	8.91	0.135	2.07	38.07	0.04	0.37	0.022	99.49	11.50
K162-9 30-106	46.37	1.11	0.015	9.65	0.146	0.54	41.43	0.03	0.32	0.043	99.66	14.46
K162-9 45-25	45.73	2.18	0.028	8.20	0.117	0.05	43.85	0.02	0.15	0.004	100.33	14.53
K162-9 58-23	46.40	3.13	0.082	10.51	0.188	2.30	36.57	0.03	0.35	0.027	99.59	11.20
K162-9 58-33	46.18	2.22	0.052	7.94	0.146	0.37	41.83	0.03	0.23	0.005	99.00	13.27
CHN35 7-92	44.30	2.39	0.068	8.10	0.160	2.47	41.19	0.10	0.45	0.029	99.26	3.96
CHN35 7-92	41.14	2.46	0.050	8.32	0.168	8.42	37.98	0.07	0.44	0.058	99.11	9.94
CHN35 7-383	44.46	2.02	0.033	9.40	0.195	0.92	42.21	0.03	0.14	0.005	99.41	1.11
CHN35 18-109	44.88	4.01	0.255	7.84	0.117	3.71	38.33	0.18	0.48	0.019	99.83	7.58
CHN35 18-287	44.15	2.95	0.223	8.69	0.127	2.80	40.27	0.15	0.24	0.062	99.66	11.04
IO11-76 60-27	46.03	2.32	0.024	7.84	0.137	0.67	42.35	0.02	0.14	0.000	99.53	11.99
IO11-76 60-51	47.56	2.46	0.029	8.89	0.128	2.35	38.11	0.06	0.32	0.011	99.92	10.32
IO11-76 60-60	45.86	1.81	0.020	8.27	0.125	0.11	43.58	0.03	0.16	0.006	99.98	13.94
IO11-76 60-165	46.42	2.07	0.020	8.37	0.121	0.21	43.06	0.02	0.19	0.005	100.49	13.85
IO11-76 60-171a	44.88	1.60	0.031	9.13	0.096	0.11	43.48	0.03	0.19	0.012	99.56	13.72
IO11-76 60-171B	46.11	2.21	0.020	8.30	0.131	0.40	42.95	0.03	0.25	0.007	100.40	13.60
VULC-5 35-37	46.58	1.87	0.020	8.78	0.118	1.85	40.70	0.04	0.19	0.008	100.15	9.97
VULC-5 41-13	46.73	3.41	0.092	8.73	0.148	2.70	38.31	0.03	0.29	0.006	100.44	11.26
VULC-5 41-29	46.60	2.38	0.050	8.78	0.130	2.37	39.58	0.04	0.22	0.017	100.16	9.17
OCE-23 14-1	44.83	2.36	0.039	9.36	0.149	4.72	37.76	0.02	0.24	0.032	99.51	9.54
OCE-23 14-3	46.05	2.31	0.036	8.69	0.164	1.48	41.14	0.02	0.14	0.006	100.03	10.92
AII107-6 40-31	46.67	1.42	0.004	9.01	0.133	1.36	41.12	0.03	0.23	0.019	99.99	13.04
AII107-6 40-46	45.71	1.32	0.005	8.43	0.131	0.08	44.25	0.03	0.16	0.006	100.12	13.75
IO11-76 60-27*	45.86	2.28	0.023	8.41	0.135	0.64	42.44	0.02	0.12	0.000	99.93	12.01
CHN35 7-92*	41.04	2.44	0.049	8.57	0.167	8.42	37.87	0.06	0.41	0.058	99.08	9.98
IO11-76 60-27**	45.72	2.28	0.025	8.43	0.135	0.65	41.97	0.02	0.14	0.000	99.37	11.97

* duplicates, **triplicates

Table S-2 cont.

Element oxides recalculated on a hydrous basis

Sample #	SiO_2 wt. %	Al_2O_3 wt. %	TiO_2 wt. %	FeO wt. %	MnO wt. %	CaO wt. %	MgO wt. %	K_2O wt. %	Na_2O wt. %	P_2O_5 wt. %	Total wt. %	
K162-9 30-105	**41.61**	2.61	0.05	7.89	0.12	1.84	33.84	0.04	0.33	0.02	88.35	
K162-9 45-25	40.19	1.92	0.02	7.21	0.10	0.04	38.54	0.02	0.13	0.00	88.17	
K162-9 58-23	42.43	2.86	0.07	9.61	0.17	2.10	33.44	0.03	0.32	0.02	91.06	
K162-9 58-33	40.93	1.97	0.05	7.04	0.13	0.33	37.07	0.03	0.20	0.00	87.74	
CHN35 7-15	42.63	2.30	0.07	7.80	0.15	2.38	39.64	0.10	0.43	0.03	95.52	
CHN35 7-92	36.98	2.21	0.04	7.60	0.15	7.58	34.13	0.06	0.38	0.05	89.19	
CHN35 7-383	43.78	1.99	0.03	9.26	0.19	0.91	41.57	0.03	0.14	0.00	97.90	
CHN35 18-109	41.57	3.71	0.24	7.27	0.11	3.44	35.50	0.17	0.44	0.02	92.47	
CHN35 18-287	39.33	2.63	0.20	7.74	0.11	2.49	35.87	0.13	0.21	0.06	88.78	
IO11-76 60-27	40.74	2.04	0.02	7.31	0.12	0.58	37.52	0.02	0.12	bd	88.46	
IO11-76 60-51	43.07	2.23	0.03	8.05	0.12	2.13	34.51	0.05	0.29	0.01	90.48	
IO11-76 60-60	39.99	1.58	0.02	7.22	0.11	0.10	38.01	0.03	0.14	0.01	87.19	
IO11-76 60-165	40.36	1.80	0.02	7.28	0.11	0.18	37.44	0.02	0.17	0.00	87.38	
IO11-76 60-171a	38.88	1.39	0.03	7.91	0.08	0.10	37.67	0.03	0.16	0.01	86.25	
IO11-76 60-171b	40.17	1.93	0.02	7.23	0.11	0.35	37.42	0.03	0.22	0.01	87.47	
VULC-5 35-37	42.16	1.69	0.02	7.94	0.11	1.67	36.84	0.04	0.17	0.01	90.64	
VULC-5 41-13	41.85	3.05	0.08	7.82	0.13	2.42	34.31	0.03	0.26	0.01	89.95	
VULC-5 41-29	42.51	2.17	0.04	7.96	0.12	2.17	36.21	0.04	0.21	0.02	91.45	
OCE-23 14-1	40.89	2.15	0.04	8.54	0.14	4.31	34.44	0.02	0.22	0.03	90.77	
OCE-23 14-3	41.03	2.06	0.03	7.74	0.15	1.32	36.65	0.02	0.12	0.01	89.12	
AII107-6 40-31	40.89	1.24	0.00	7.89	0.12	1.19	36.03	0.03	0.20	0.02	87.62	
AII107-6 40-46	39.91	1.15	0.00	7.36	0.11	0.07	38.64	0.03	0.14	0.01	87.42	

Supplementary Information References

Downs, R.T. (2006) The RRUFF Project: an integrated study of the chemistry, crystallography, Raman and infrared spectroscopy of minerals. Program and Abstracts of the 19th General Meeting of the International Mineralogical Association in Kobe, Japan. O03-13 2006.

Földvári, M. (2011) *Handbook of the thermogravimetric system of minerals and its use in geological practice*. Geological Institute of Hungary, Budapest.

Gualtieri, A.F., Giacobbe, C., Viti, C. (2012) The dehydroxylation of serpentine group minerals. *American Mineralogist* 97, 666–680.

Hart, S.R., Zindler, A. (1986) In search of a bulk-Earth composition. *Chemical Geology* 57, 247–267.

Jagoutz, E., Palme, H., Baddenhausen, H., Blum, K., Cendales, M., Dreibus, G., Spettel, B., Lorenz, V., Wanke, H. (1979) The abundances of major, minor and trace elements in the earth's mantle as derived from primitive ultramafic nodules. *Lunar and Planetary Inst.~Technical Report*, 610–612.

Johnson, D.M., Hooper, P.R., Conrey, R.M. (1999) XRF Analysis of Rocks and Minerals for Major and Trace Elements on a Single Low Dilution Li-tetraborate Fused Bead. *Advances in X-ray Analysis, v, 41, p. 843–867 Le Bas, M.J.*

Johnson, J.W., Oelkers, E.H., Helgeson, H.C. (1992) SUPCRT92: A software package for calculating the standard molal thermodynamic properties of minerals, gases, aqueous species, and reactions from 1-5000 bars and 0-1000°C. *Computers & Geosciences* 18, 899–947.

Kahl, W.-A., Jöns, N., Bach, W., Klein, F., Alt, J.C. (2015) Ultramafic clasts from the South Chamorro serpentine mud volcano reveal a polyphase serpentinization history of the Mariana forearc mantle. *Lithos* 227, 1–20.

Klein, F., Bach, W., Jöns, N., McCollom, T., Moskowitz, B., Berquó, T. (2009) Iron partitioning and hydrogen generation during serpentinization of abyssal peridotites from 15°N on the Mid-Atlantic Ridge. *Geochimica et Cosmochimica Acta* 73, 6868–6893.

Klein, F., Bach, W., McCollom, T.M. (2013) Compositional controls on hydrogen generation during serpentinization of ultramafic rocks. *Lithos* 178, 55–69.

Klein, F., Bach, W., Humphris, S.E., Kahl, W.-A., Jöns, N., Moskowitz, B., Berquó, T.S. (2014) Magnetite in seafloor serpentinite - Some like it hot. *Geology* 42, 135–138.

Klein, F., Humphris, S.E., Marschall, H.R., Bowring, S.A., Horning, G. (2017) Mid-ocean ridge serpentinite in the Puerto Rico Trench: from seafloor spreading to subduction. *Journal of Petrology* 58, 1729–1754.

Lafay, R., Montes-Hernandez, G., Janots, E., Chiriac, R., Findling, N., Toche, F. (2012) Mineral replacement rate of olivine by chrysotile and brucite under high alkaline conditions. *Journal of Crystal Growth* 347, 62–72.

Nielsen, S.G., Klein, F., Kading, T., Blusztajn, J., Wickham, K. (2015) Thallium as a tracer of fluid-rock interaction in the shallow Mariana forearc. *Earth and Planetary Science Letters* 416–426.

Okamoto, A., Ogasawara, Y., Ogawa, Y., Tsuchiya, N. (2011) Progress of hydration reactions in olivine-H_2O and orthopyroxenite-H_2O systems at 250 °C and vapor-saturated pressure. *Chemical Geology* 289, 245–255.

Paulick, H., Bach, W., Godard, M., de Hoog, J.C.M., Suhr, G., Harvey, J. (2006) Geochemistry of abyssal peridotites (Mid-Atlantic Ridge, 15°20'N, ODP Leg 209): implications for fluid-rock interaction in slow spreading environments. *Chemical Geology* 234, 179–210.

Petriglieri, J.R., Salvioli-Mariani, E., Mantovani, L., Tribaudino, M., Lottici, P.P., Laporte-Magoni, C., Bersani, D. (2015) Micro-Raman mapping of the polymorphs of serpentine. *Journal of Raman Spectroscopy* 46, 953–958.